Tetragonal Phase Germanium Nanocrystals in Lithium Ion Batteries

Yong Jae Cho,[†] Hyung Soon Im,[†] Han Sung Kim,[†] Yoon Myung,[†] Seung Hyuk Back,[†] Young Rok Lim,[†] Chan Su Jung,[†] Dong Myung Jang,[†] Jeunghee Park,[†,*] Eun Hee Cha,[‡] Won Il Cho,[§] Fazel Shojaei,[⊥] and Hong Seok Kang[∥,*]

[†]Department of Chemistry, Korea University, Jochiwon 339-700, Korea, [‡]Department of Liberal Art and Literature, Hoseo University, Chungnam 336-795, Korea, [§]Center for Energy Convergence, Korea Institute of Science and Technology, Seoul 136-791, Korea, [⊥]Department of Chemistry, Jeonbuk National University, Chonju, Chonbuk 560-756, Korea, and [∥]Department of Nano and Advanced Materials, College of Engineering, Jeonju University, Chonju, Chonbuk 560-759, Korea

ABSTRACT Various germanium-based nanostructures have recently demonstrated outstanding lithium ion storage ability and are being considered as the most promising candidates to substitute current carbonaceous anodes of lithium ion batteries. However, there is limited understanding of their structure and phase evolution during discharge/charge cycles. Furthermore, the theoretical model of lithium insertion still remains a challenging issue. Herein, we performed comparative studies on the cycle-dependent lithiation/delithiation processes of germanium (Ge), germanium sulfide (GeS), and germanium oxide (GeO_2) nanocrystals (NCs). We synthesized the NCs using a convenient gas phase laser photolysis reaction and attained an excellent reversible capacity: 1100−1220 mAh/g after 100 cycles. Remarkably, metastable tetragonal (ST12) phase Ge NCs were constantly produced upon lithiation and became the dominant phase after a few cycles, completely replacing the original phase. The crystalline ST12 phase persisted through 100 cycles. First-principles calculations on polymorphic lithium-intercalated structures proposed that the ST12 phase $Ge_{12}Li_x$ structures at $x \geq 4$ become more thermodynamically stable than the cubic phase Ge_8Li_x structures with the same stoichiometry. The production and persistence of the ST12 phase can be attributed to a stronger binding interaction of the lithium atoms compared to the cubic phase, which enhanced the cycling performance.

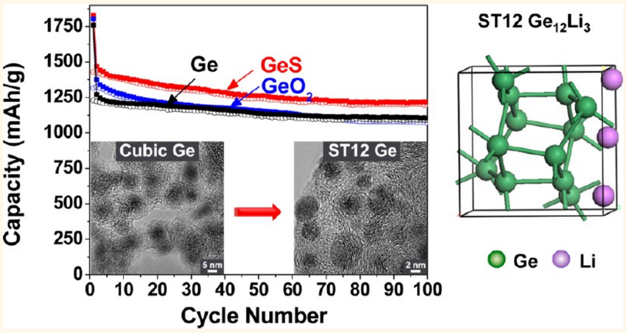

KEYWORDS: germanium · tetragonal structures · phase conversion · lithium ion batteries · first-principles calculations · lithium-intercalated polymorphs

Germanium (Ge) is considered to be the most promising candidate for an alternative material in commercial carbonaceous anodes for lithium ion batteries (LIBs).[1,2] The bulk phase is known to have a higher theoretical capacity (1620 mAh/g) than graphite carbon (370 mAh/g), owing to lithium (Li) alloy formation (*i.e.*, $Li_{22}Ge_5$). However, large volume changes (up to 300%) during lithiation/delithiation can lead to capacity fading. It is assumed that the amorphization of Ge during lithiation could have a significant impact on mechanical stress generation and disintegration. To overcome this problem, various nanostructures have been developed by a number of research groups.[3−21] Their high surface to volume ratio minimizes the volume change and dissipates the mechanical stress. It also increases the electrode/electrolyte interface area and promotes faster diffusion of Li^+ ions within the material, increasing the charging rate.

One mitigating strategy is to encapsulate nanostructures in a conducting buffer matrix to minimize volume change and dissipate the mechanical stress inside the matrix. This has been shown to work well for carbon (C) shell coating or hosting. The use of an oxide or sulfide compound has been suggested as another approach. In that case, the oxygen or sulfur is able to provide a matrix with high Li^+ ion conductivity, thereby reducing internal resistance.[6,20,22,23] GeS and GeO_2 are irreversibly converted to Ge in the first cycle of use, according to eq 1 below. Subsequently, Ge can store and release Li ions according to the Li−Ge alloying and dealloying reactions

* Address correspondence to parkjh@korea.ac.kr, hsk@jj.ac.kr.

Received for review July 17, 2013 and accepted September 10, 2013.

10.1021/nn403674z

shown in eq 2.

$$\mathrm{GeS} + 2\mathrm{Li}^+ + 2e^- \rightarrow \mathrm{Ge} + \mathrm{Li_2S} \quad \text{or}$$
$$\mathrm{GeO_2} + 4\mathrm{Li}^+ + 4e^- \rightarrow \mathrm{Ge} + 2\mathrm{Li_2O} \qquad (1)$$

$$\mathrm{Ge} + x\mathrm{Li}^+ + xe^- \leftrightarrow \mathrm{Li}_x\mathrm{Ge} \quad (0 \leq x \leq 4.4) \qquad (2)$$

An important step for controlling the reversible alloying/dealloying between Li and Ge is a clear understanding of the structure and phase changes. This information is paramount for predicting stresses, interface energies, and diffusion rates within the materials. In our recent work, the production of metastable tetragonal phase (ST12) Ge nanocrystals (NCs) was discovered.[23] The ST12 Ge NCs formed after the first discharge (lithiation) of both amorphous and crystalline GeS (and GeS_2) nanoparticles and persisted even after 100 cycles. This result raises a question as to the production of ST12 phase during lithiation of Ge and GeO_2. In the present work, well-known Ge-based NCs, Ge, GeS, and GeO_2, were synthesized using a gas phase laser photolysis reaction and then used as the anode materials for the development of high-performance LIBs. Remarkably, the ST12 phase Ge NCs were all produced from the lithiation process. First-principles calculations were performed on the intercalation of various numbers of Li atoms into the ST12 and cubic phase Ge lattices. The results suggested that the ST12 phase increases the capacity of Li intercalation compared to the cubic phase because of the stronger binding interactions of Li atoms. To the best of our knowledge, this is the first theoretical study on Li-intercalated Ge polymorphs, and this study helps rationalize experimental results.

RESULTS AND DISCUSSION

The synthesis procedures are briefly described as follows. The photolysis of tetramethyl germanium (TMG) produced Ge NCs, and the addition of H_2S in a 1:1 ratio during photolysis induced formation of amorphous GeS.[23] Thermal annealing at 450 °C produced crystalline GeS NCs. The GeO_2 NCs were synthesized by oxidation of Ge NCs at 600 °C under ambient O_2. XRD patterns confirmed cubic Ge (JCPDS No. 04-0545; a = 5.6576 Å), orthorhombic GeS (JCPDS No. 85-1114; a = 4.290 Å, b = 10.42 Å, c = 3.640 Å), and hexagonal GeO_2 (JCPDS No. 85-1515; a = 4.985 Å, c = 5.647 Å), as shown in the Supporting Information (SI), Figure S1.

Figure 1a shows the high-resolution TEM (HRTEM) image of Ge NCs. They have a homogeneous size distribution with an average value of 7 nm. The Ge NCs are sheathed with 1−2 nm thick graphitic C layers. The lattice-resolved image of an individual NC and the corresponding fast Fourier transform (FFT) image at the [011] zone axis confirm that the *d*-spacing of the faced-centered cubic (111) planes is about 3.3 Å, which is consistent with the value of bulk Ge (Figure 1b). The C content was estimated to be about 15 wt %.[18] Before annealing, amorphous GeS nanoparticles (with negligible C layers) have a spherical shape and an average diameter of 10 nm. Thermal annealing produces the single-crystalline GeS NCs with enlarged size (10−20 nm), as shown in the HRTEM image of Figure 1c. The lattice-resolved and FFT images of the orthorhombic GeS NCs reveal that the *d*-spacing of the (120) planes is 3.3 Å, which is consistent with bulk GeS (Figure 1d). The single-crystalline GeO_2 NC (diameter = 10−20 nm) typically agglomerated into clusters with random sizes up to 100 nm. The C layers became negligible after the O_2 oxidation process at 600 °C. The lattice-resolved and corresponding FFT images of GeO_2 NC showed that the *d*-spacing of the (011) planes is 3.4 Å, corresponding to hexagonal phase GeO_2 (Figure 1e). The EDX data for individual NCs are shown in the SI, Figure S2.

The discharge/charge capacities of a half-cell containing Ge, GeS, and GeO_2 NCs as active anode materials for LIBs were measured. Figure 2a shows their capacity as a function of the cycle number up to 100 cycles at a rate of 160 mA/g, between 0.01 and 1.5 V. For all three materials, 1 C was defined as the theoretical capacity of pure Ge. In fact, the theoretical capacity of Ge NC could be 1380 mAh/g, considering that the specific capacity calculation included the C component, which is 15 wt %. The theoretical 4.4 Li insertion capacity of GeS and GeO_2 was calculated as 1130 mAh/g. Ge, GeS, and GeO_2 exhibited discharge capacities as high as 1100, 1220, and 1090 mAh/g after 100 cycles, respectively. These values reach 80, 108, and 96% of the theoretical capacity. All cells exhibited reversible capacities with high Coulombic efficiency (avg 99%) after the first cycle. Voltage profiles and cyclic voltammetry curves are shown in the SI, Figures S3 and S4, respectively.

The first discharge and charge capacities of Ge were 1760 and 1230 mAh/g, respectively, with an initial Coulombic efficiency of 70%. This initial capacity loss can be attributed to the formation of solid electrolyte interphase (SEI) layers on the electrode surface during Li storage, similar to that reported in previous works.[3−21] After the first cycle, the Ge cell exhibits excellent reversibility of capacity with an average Coulombic efficiency of 98.4% up to 100 cycles. The first discharge and charge capacities of GeS were 1830 and 1430 mAh/g, respectively, with an initial Coulombic efficiency of 78%. The first discharge/charge capacities for GeO_2 are 1760/1230 mAh/g, and the initial Coulombic efficiency is 70%. This initial capacity loss from GeS and GeO_2 could be attributed to their irreversible decomposition into Ge and Li_2S (or Li_2O). After the first cycle, the GeS and GeO_2 achieved nearly complete capacity reversibility, with an average Coulombic efficiency of 98.7 and 98.8% up to 100 cycles, respectively.

The rate capabilities of the NCs were tested by sequentially measuring the capacity as the discharge/charge

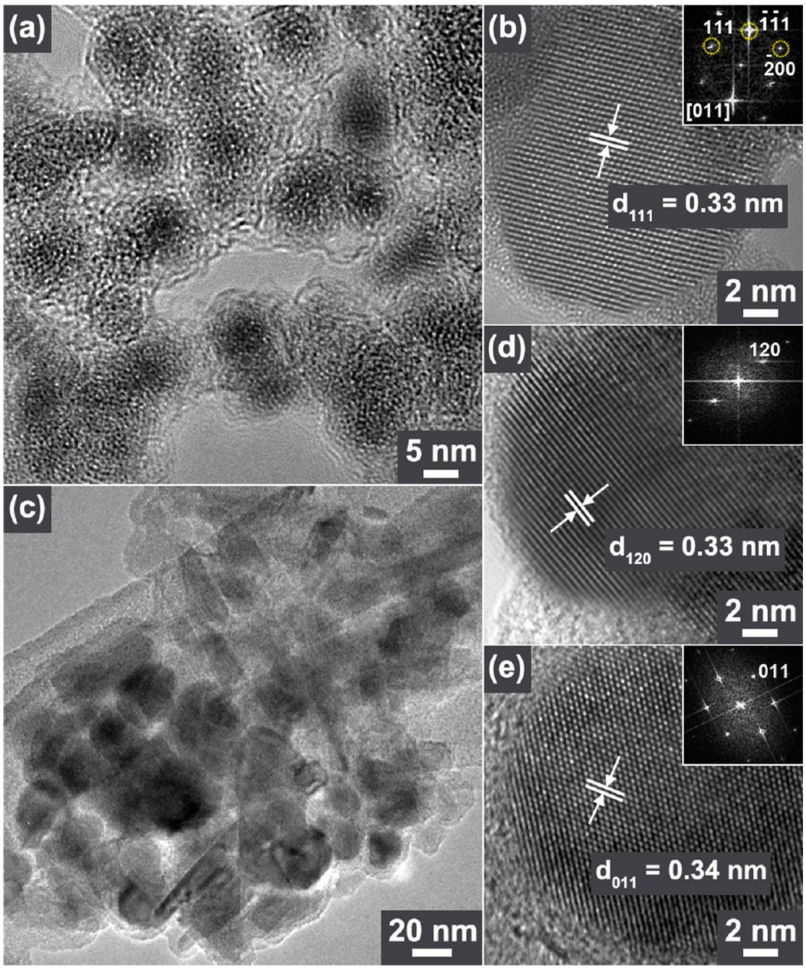

Figure 1. **(a) HRTEM image showing the general morphology of Ge NC (avg diameter = 7 nm). The graphitic layers surround the spherical NC with a thickness of 1−2 nm. (b) Lattice-resolved and FFT images (zone axis of cubic phase = [011]) of selected Ge NCs. The *d*-spacing of the cubic phase (111) planes is 3.3 Å. (c) HRTEM image showing the general morphology of GeS NC, and its (d) lattice-resolved and FFT images revealing that the *d*-spacing of orthorhombic phase GeS (120) planes is 3.3 Å. (e) Lattice-resolved and corresponding FFT images of single-crystalline hexagonal phase GeO_2 NC (d_{011} = 3.4 Å).**

rates increased from 0.1 C to 0.2, 0.5, 1.0, 2.0, and 5.0 C, and then returned to 0.1 C, as shown in Figure 2b. When the rate was increased to 1.0 C, a small decrease in discharge capacity was observed from 1200 to 1140 mAh/g for Ge, from 1410 to 1240 mAh/g for GeS, and from 1330 to 1080 mAh/g for GeO_2. Upon a further increase to 5.0 C, the discharge capacity of GeS decreased slightly to 1110 mAh/g. In contrast, Ge and GeO_2 decreased more significantly to 550 and 620 mAh/g, respectively. When the rate returned to 0.1 C (after 60 cycles), the discharge capacity increased back to 90% (avg) of the initial capacity. It can be concluded that all of the NCs have excellent capacity stability even after going through cycles at higher rates. The GeS NCs not only have a higher capacity but also have higher rate capabilities than the Ge and GeO_2 NCs.

Ex situ XRD measurements were done to investigate the phase change during the lithiation/delithiation processes (Figure 3). The XRD peaks of the as-prepared electrode prior to the cycling tests matched the peaks of cubic phase Ge, orthorhombic phase GeS, and hexagonal phase GeO_2. The peaks in the range 2θ = 15−40° were only analyzed to avoid the stronger peak from the Cu foil electrode at 2θ = 43.3°. As the Ge cell was first discharged to 0.01 V (lithiation), new peaks (marked by the blue slash filling) emerged at 19.9, 23.1, 25.8, and 39.0°. These peaks were a match for the (211), (220), (310), and (332) planes of the cubic phase of $Li_{15}Ge_4$ (JCPDS No. 89-2584; a = 10.7860 Å). After a full charge to 1.5 V (delithiation), only the cubic phase Ge peaks remained. In the third discharged cell, the $Li_{15}Ge_4$ peaks became dominant while the cubic Ge peaks virtually disappeared. After the fifth discharge, the $Li_{15}Ge_4$ peaks disappeared, but new peaks at 20.1, 32.3, and 35.6° became a major feature. In the third and fifth charged cells, only amorphous phase remained. However, as the number of cycles increased, the three peaks persisted, even in the charged cells (see the 10th and 100th charged cells). It was possible to assign these three peaks (marked by the red slash filling) to the (110), (201), and (211) planes of tetragonal ST12 phase Ge (JCPDS No. 72-1425; $a = 5.93$ Å and $c = 6.98$ Å), respectively. The ST12 phase is known to be a metastable semiconductor (E_g = 1.47 eV). While it was initially discovered by compressing cubic phase Ge at high pressure, it has also recently been identified at ambient pressure and temperature.[24−27] The (110), (201), and (211) peaks shifted to a lower angle by 1.0, 0.5, and 0.5° from the reference, respectively, indicating an expansion of the lattice constants. The increase in the *d*-spacing of the (110) planes was calculated to be 5%, which is more significant than the ~2% of the (201) and (211) planes.

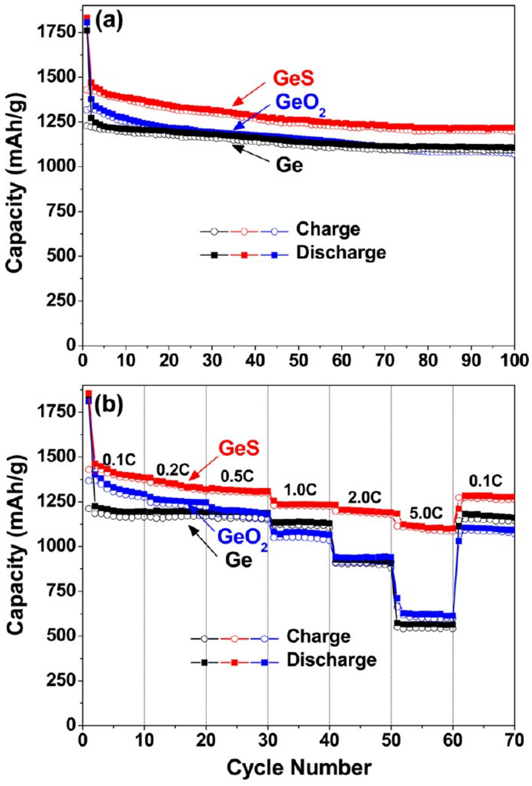

Figure 2. (a) Discharge/charge capacity *versus* cycle number (1−100) for half-cells of Ge, GeS, and GeO$_2$ NCs with a rate of 0.1 C. (b) Cycling performance as the rate increases from 0.1 to 5.0 C and returns to 0.1 C.

In the case of GeS, the ST12 Ge peaks (marked by the red slash filling) emerged after the first discharge. The GeS peaks in the first discharged/charged cells indicated that all the GeS did not decompose into Ge. In the third discharged cell, the (110), (201), and (211) peaks of the ST12 phase became significant, while the GeS peak disappeared completely. No other peaks related to the cubic phase Ge or Li−Ge alloy (such as $Li_{15}Ge_4$) were detected. The ST12 peaks remained in the charged cell at a reduced intensity. As the cycle number increased, the peak intensity gradually decreased and peak width increased. Nevertheless, the ST12 phase persisted for up to 100 cycles in both discharged and charged cells. For the GeO$_2$ cells, the ST12 Ge peaks also emerged during the first discharge and became a major feature in the third discharged cell. After the fifth discharge, the GeO$_2$ phase disappeared and only the ST12 phase existed. The ST12 phase remained in the 100th charged cell, which is identical behavior to Ge and GeS. The GeS exhibits a stronger ST12 peak intensity over the whole 100 cycles than Ge and GeO$_2$.

HRTEM images confirmed the persistence of ST12 phase Ge NCs in the fully charged GeS cell after 100 cycles (Figure 4a). The Ge NCs are usually embedded in the carbon/amorphous matrix. The average diameter is about 5 nm, which is smaller than that of GeS NCs. Figure 4b corresponds to the scanning TEM (STEM; dark-field TEM) image. The crystalline Ge NCs (white spots) are well-dispersed in the amorphous matrix (gray background). The *d*-spacing of the (113) planes

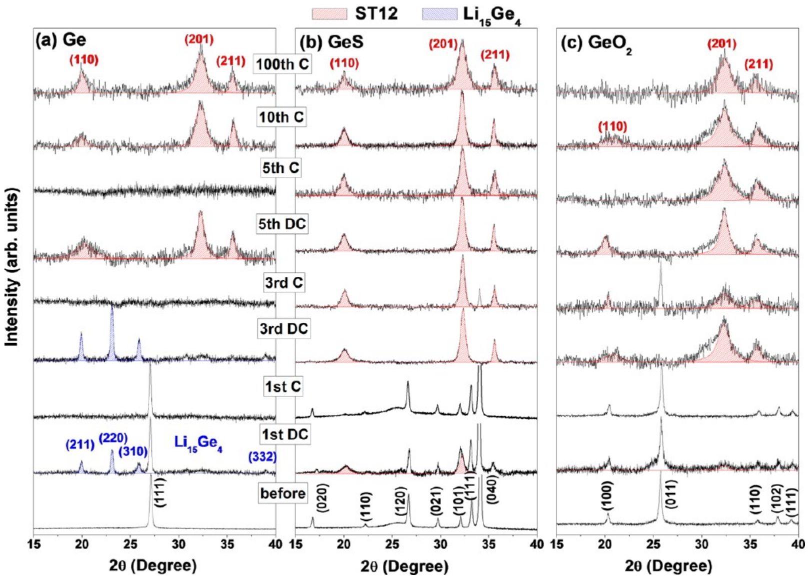

Figure 3. XRD pattern of (a) Ge, (b) GeS, and (c) GeO$_2$ electrodes before and after the 1st, 3rd, 5th, 10th, and 100th discharge (DC)/charge (C) cycles.

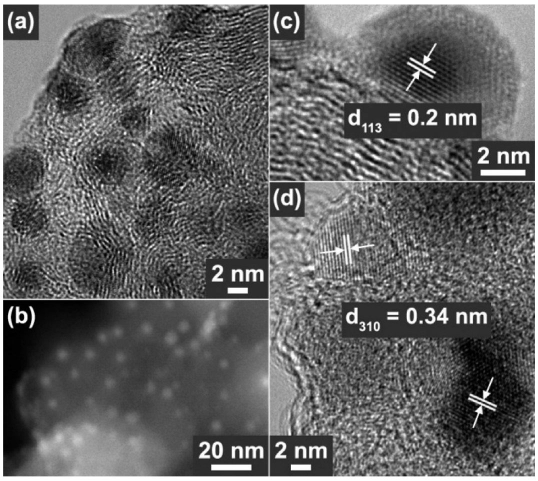

Figure 4. (a) HRTEM and (b) STEM images of ST12 phase Ge NCs (sampled from the fully charged GeS cell after 100 cycles) embedded in the carbon/amorphous matrix. (c) The *d*-spacing of the ST12 Ge (113) planes is 2.0 Å. (d) HRTEM image of cubic phase L$_{15}$Ge$_4$ NCs (sampled after the third fully discharged Ge cell), clearly showing the (310) planes with *d*-spacing of 3.4 Å.

is 2.0 Å, which is close to that of ST12 phase Ge (Figure 4c). The existence of cubic phase L$_{15}$Ge$_4$ NCs from the third discharged Ge cell was also confirmed (Figure 4d). The *d*-spacing of the (310) planes is 3.4 Å, which is close to that of the reference, d_{310} = 3.411 Å.

Previous *in situ* and *ex situ* XRD studies showed that Ge becomes amorphous during the first lithiation, and that the highly lithiated amorphous Li$_x$Ge mainly crystallizes into cubic Li$_{15}$Ge$_4$.[28,29] This result is similar to that of Si, which crystallizes into Li$_{15}$Si$_4$.[30] The Huang group reported on *in situ* TEM of individual Ge nanowires and confirmed the two-step phase transformation process of lithiation: formation of the intermediate amorphous Li$_x$Ge and the crystalline Li$_{15}$Ge$_4$ phase.[31] In contrast to the size-dependent fracturing of Si, Ge remains robust without any visible fractures or cracking even with a volume change of ~260%.[32−34] The Ge nanowires develop a spongy-like network that can mitigate large volume changes during lithiation and delithiation.

The present Ge NC results show that the Li insertion produced crystalline Li$_{15}$Ge$_4$ up to the third cycle, which agrees well with previous work.[28,29] However, when no cubic phase Ge (or only the amorphous phase) is left, no Li$_{15}$Ge$_4$ phase was produced upon lithiation, as shown in the third charged and fifth discharged cells. Instead, the crystalline ST12 phase emerged during the lithiation and persisted even after 100 cycles. To the best of our knowledge, this remarkable ST12 phase, produced from the Li insertion of Ge NCs, has not yet been reported. The production of the ST12 phase can be attributed to the thermodynamic stability of the Li-intercalated structures, which is discussed later using calculations. The maintenance of the crystalline ST12 phase over many cycles may be correlated to the tough feature of the Ge nanostructures observed by *in situ* TEM.[31,32]

Lithiation kinetics in a single-crystal Si matrix are highly anisotropic. Cui and co-workers studied the anisotropic volumetric expansion of crystalline Si nanopillars, and they showed that the volume expansion of the lithiated Si is vastly more favorable for the ⟨110⟩ direction than the ⟨111⟩ direction.[35] *In situ* TEMs have consistently shown significant swelling along the ⟨110⟩ direction but negligible swelling along the ⟨111⟩ direction if both faces are exposed.[33] Various reasons, based on thermodynamic, kinetic, and mechanical models, have been offered as possible explanations for this anisotropic effect.[36−39] Yassar and co-workers reported *in situ* TEM images of lithiated SnO$_2$ nanowires, indicating that the lithium ions' initial preference to diffuse along the [001] direction in the {200} planes of rutile (tetragonal) phase SnO$_2$ introduced the lattice expansion.[40] Here, the lattice expansion of the ST12 phase Ge NCs would be due to Li insertion in the Ge lattices. The more expanded (110) planes (compared to the (201) and (211) planes) suggest the anisotropic Li intercalation in the Ge lattices of the ST12 phase. The following calculations show that the anisotropic expansion of lattice constants is because of the preferred Li intercalation on the (100) planes.

The Li insertion of GeS (or GeO$_2$) NCs proceeds *via* an irreversible transformation to Ge and amorphous Li$_2$S (or Li$_2$O), and this mechanism was supported by LIB data. The XRD results suggest that the ST12 phase Ge can be directly produced from the decomposition of GeS and GeO$_2$, not through the cubic phase Ge. The better cycling performance of GeS compared to Ge and GeO$_2$ could be attributed to a more efficient production and persistence of the ST12 phase. The CV curve of GeS shows consistently the stronger lithitation peak near 0.35 V (corresponding to crystalline phase Ge[41,42]) compared to that of Ge and GeO$_2$ (see SI, Figure S4). The high concentration Li insertion likely transformed most of the ST12 Ge into amorphous Li$_x$Ge alloys, but some portion still existed in the crystalline form, which was detected by XRD analysis. It is expected that retaining the crystalline phase increases the electrical conductivity compared to the amorphous phase, leading to a capacity enhancement, especially at the higher discharge/charge rates. Disintegration of the crystalline ST12 phase inevitably takes place with the cycle number, so the capacity decreases gradually. Therefore, it was concluded that the favorable production and persistence of the ST12 phase promises enhanced cycling performance.

To explain how the ST12 phase Ge NCs formed upon lithiation, the following calculations were performed. The Li atoms were added into the ST12 phase of Ge by the following pathways: from Ge$_{12}$ to Ge$_{12}$Li$_3$, Ge$_{12}$Li$_4$, Ge$_{12}$Li$_6$, and Ge$_{12}$Li$_8$ (Ge$_{12}$ → Ge$_{12}$Li$_3$ → Ge$_{12}$Li$_4$ → Ge$_{12}$Li$_6$ → Ge$_{12}$Li$_8$). Table 1 lists the following

TABLE 1. Parameters for Li Intercalation Reaction of ST12 Phase Ge and Diamond Phase Ge

Li intercalation reaction	N^a	$(a = b, c)$ in Å^b	E_b^1 (eV)^c	V^1 (Å^3)^d	δV (%)^e	E_{tot} (eV)^f
Ge_{12}(ST12)	1	(6.06, 7.12)				−52.242 (−34.828)^g
$Ge_{12} + 3Li \rightarrow Ge_{12}Li_3$	4	(6.36, 7.02)	−0.34	94.7	9	−58.899 (−39.266)
$Ge_{12}Li_3 + Li \rightarrow Ge_{12}Li_4$	4	(6.62, 7.10)	−0.94	77.8	10	−61.715 (−41.143)
$Ge_{12}Li_4 + 2Li \rightarrow Ge_{12}Li_6$	3	(6.74, 7.46)	−0.78	56.5	9	−67.022 (−44.681)
$Ge_{12}Li_6 + 2Li \rightarrow Ge_{12}Li_8$	3	(6.83, 7.81)	−0.56	45.5	7	−71.888 (−47.925)
Ge_8(diamond)	1	(5.78, 5.78)				−35.941
$Ge_8 + 2Li \rightarrow Ge_8Li_2$(tetragonal)	2	(6.19, 5.73)	0.12	109.7	13	−39.435
$Ge_8Li_2 + Li \rightarrow Ge_8Li_3$	2	(6.37, 5.61)	−0.26	75.9	4	−41.547
$Ge_8Li_3 + Li \rightarrow Ge_8Li_4$	4	(5.81, 7.05)	−0.54	59.5	4	−43.964
$Ge_8Li_4 + Li \rightarrow Ge_8Li_5$	2	(5.80, 7.25)	−0.68	48.8	3	−46.511
$Ge_8Li_5 + Li \rightarrow Ge_8Li_6$	3	(5.84, 7.46)	−0.76	42.4	4	−49.146

[a] Number of configurations considered. [b] Lattice constants ($a = b, c$). [c] Energy change of the Li intercalation per Li atom. [d] Volume per Li atom (V^1) of product. [e] Volume change accompanying the Li intercalation. [f] Total energy of the most stable configuration of reaction products. [g] The 2/3 value of E_{tot} for Li-intercalated ST12 phase.

parameters for the stepwise Li insertion reactions: the number of configurations considered (N), the lattice constants ($a = b$, c), the energy change of the Li intercalation per Li atom (E_b^1), the volume of the Li-intercalated products per Li atom (V^1), the volume increase accompanying the Li intercalation (δV), and the total energy of the most stable configuration (E_{tot}). For each step, three to four initial configurations were considered by inserting appropriate number of Li atoms. For example, four different initial configurations of $Ge_{12}Li_4$ were considered for the $Ge_{12}Li_3 + Li \rightarrow Ge_{12}Li_4$ process, where one Li atom is inserted into the most stable configuration of $Ge_{12}Li_3$. The geometric optimization was performed for each configuration, which consequently alters the lattice constants. The lowest-energy configuration was selected as the final configuration of $Ge_{12}Li_4$. The structures of Ge_{12}, $Ge_{12}Li_3$, $Ge_{12}Li_4$, and $Ge_{12}Li_6$, projected onto the *ab* and *ac* planes, are shown in Figure 5. In $Ge_{12}Li_3$, three Li atoms lie on (100) plane, and most of the chemical bonds between the Ge atoms remain intact upon the Li insertion. The $Ge_{12}Li_4$ and $Ge_{12}Li_6$ lattices mostly maintain the ST12 structure. However, Li insertion at $x \geq 8$ results in amorphization (data not shown here).

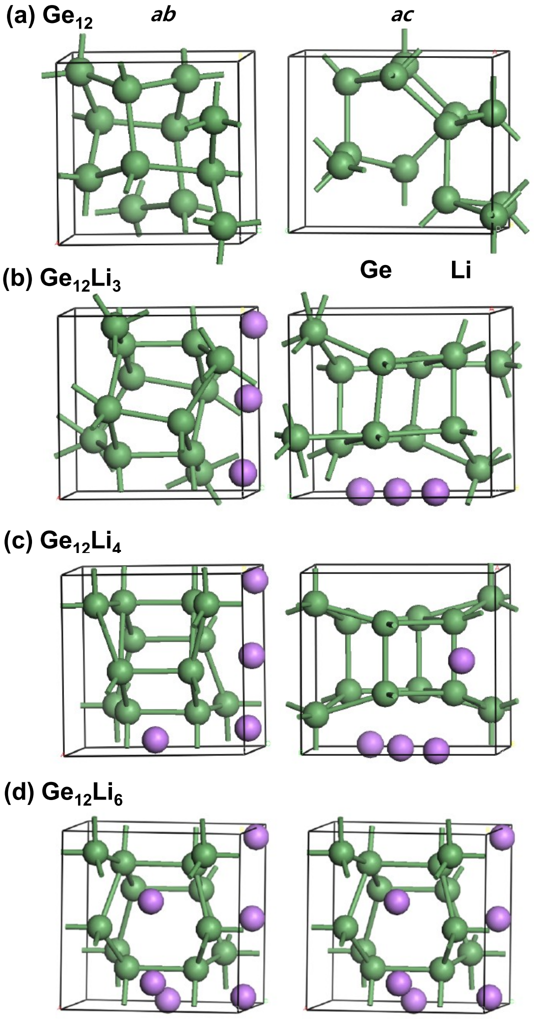

Figure 5. Structure of (a) Ge_{12} (ST12), (b) $Ge_{12}Li_3$, (c) $Ge_{12}Li_4$, and (d) $Ge_{12}Li_6$, projected onto the *ab* and *ac* planes.

The E_b^1 values, where the superscript 1 denotes the energy change per Li atom, were found to be significantly negative for all the processes, indicating that the Li insertions up to $Ge_{12}Li_8$ are thermodynamically favored. It is highly probable that the computed configuration may not correspond to the global energy minimum at a given stoichiometry. Therefore, the E_b^1 values as well as the total energy (E_{tot}) of reaction product may be considered as the upper limit of the global energy minimum. It is worth noting that the lattice constants increase from (6.06, 7.12) to (6.36, 7.02) Å with the lithiation process of $Ge_{12} + 3Li \rightarrow Ge_{12}Li_3$, indicating that the lattice constants a and b ($a = b$) increase by ~5%, while the lattice constant c does not change by a significant amount. The anisotropic change of lattice constants is due to the intercalated Li atoms on the (100) planes, as explained above. This result is consistent with the XRD data where the d-spacing of (110) planes in the ST12 phase of Ge NCs increased by ~5%, which is more significant than those of (201) and (211) planes. Therefore, it was

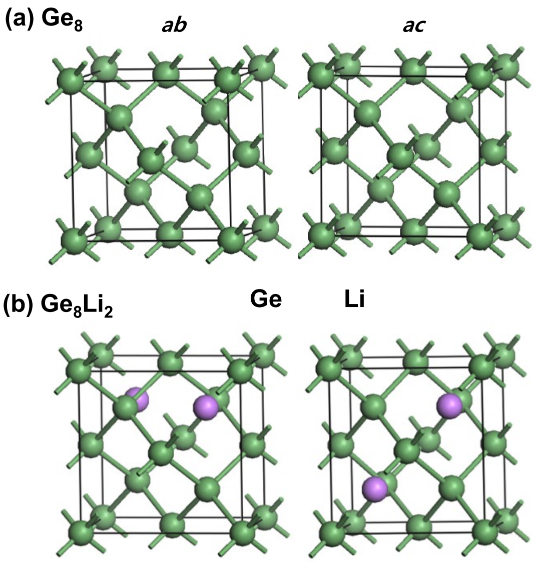

Figure 6. Structure of (a) Ge_8 (diamond) and (b) Ge_8Li_2 (tetragonal), projected onto the *ab* and *ac* planes.

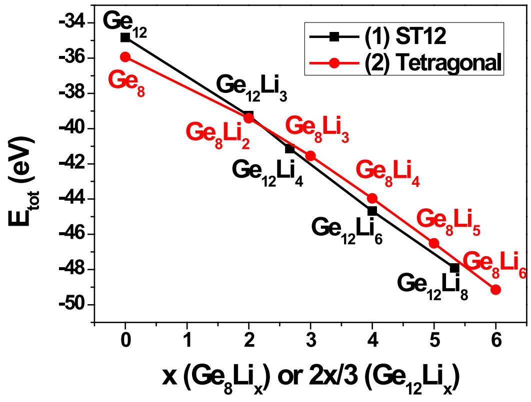

Figure 7. Total energy (E_{tot} in eV) of tetragonal phase Ge_8Li_x (produced from cubic phase Ge_8) *versus* x, and 2/3 × E_{tot} of ST12 phase $Ge_{12}Li_x$ *versus* $2x/3$.

concluded that the intercalated Li atoms caused the lattice expansion of the ST12 phase Ge NCs, which could exist as a form of $Ge_{12}Li_3$. Once they produced, the Li atoms could not be completely removed by the delithiation process because of their strong binding interactions with the Ge atoms.

Next, the cubic (diamond) phase was studied to determine if it is less stable than the ST12 phase when the Li atoms are intercalated into the Ge lattices. The Li atoms were added into the diamond phase of Ge_8 lattices by the following pathways: $Ge_8 \rightarrow Ge_8Li_2 \rightarrow Ge_8Li_3 \rightarrow Ge_8Li_4 \rightarrow Ge_8Li_5 \rightarrow Ge_{12}Li_6$. Table 1 lists all the parameters for the stepwise Li intercalation reactions of Ge_8 lattices. First, $Ge_8 + 2Li \rightarrow Ge_8Li_2$ (tetragonal) process was studied. For Ge_8Li_2, two possible *configurations A* and *B* are considered. In configuration A, both the Li atoms occupy two out of the four tetrahedral sites. After a Li atom occupies a tetrahedral site, the remaining three tetrahedral sites become equivalent. In configuration B, one Li atom occupies a tetrahedral site, while the other Li atom occupies an octahedral site. No other configurations are possible. The calculation result shows that configuration A is more stable than configuration B by 0.13 eV. Therefore, it is highly probable that configuration A corresponds to the global energy minimum.

A comparison of the lattice parameters of Ge_8 and Ge_8Li_2 shows that the diamond structure of Ge_8 transforms into the tetragonal structure Ge_8Li_2 without the cleavage of any Ge−Ge bond. The structures of Ge_8 and Ge_8Li_2 are shown in Figure 6. The Li insertion into the diamond phase is much less favored than that in the ST12 phase. This is manifested in the positive value (0.13 eV) of E_b^1 (Ge_8, 2 Li), which is very different from the negative value (−0.34 eV) of E_b^1 (Ge_{12}, 3 Li). Therefore, the Li atoms could be easily inserted into the weaker Ge−Ge bond of the ST12 structure to form $Ge_{12}Li_3$, while a process leading to the same stoichiometric diamond structure of Ge_8Li_2 is less favored. In other words, the delithiation of Ge_8Li_2 is thermodynamically favored, while that of $Ge_{12}Li_3$ is not thermodynamically favored. This observation supports our previous assumption that the Li atoms cannot be completely removed during the delithiation of the ST12 phase.

Next, the stepwise Li insertions to produce Ge_8Li_3 and Ge_8Li_4 were studied. Two possible configurations A and B for Ge_8Li_3 and Ge_8Li_4 were considered: (i) one Li atom in the unoccupied tetrahedral sites for configuration A and (ii) one Li atom in the octahedral sites for configuration B. No other configuration seems to be possible. The former configuration was found to be more stable than the latter by 0.10 eV for both stoichiometries, suggesting that configuration A presumably corresponded to the global energy minimum structure. Although the structures are not shown here, the diamond structure was perfectly preserved. Next, $Ge_8Li_4 + Li \rightarrow Ge_8Li_5$ process was studied, in which one additional Li atom was placed in the octahedral site, as no other options were available. Therefore, this configuration presumably corresponded to the global energy minimum. In this configuration, all the tetrahedral and octahedral sites are filled. Finally, the $Ge_8Li_5 + Li \rightarrow Ge_8Li_6$ process was studied. The most stable configuration was formed when the Li atom was inserted in a position close to a tetragonal site rather than to an octahedral site. The E_b^1 value is larger than those of previous steps at the lower stoichiometries, indicating that the Li insertion becomes more favorable at a higher Li composition.

Figure 7 shows the total energy (E_{tot}) of tetragonal phase Ge_8Li_x (produced from diamond phase Ge_8) and 2/3 × E_{tot} of ST12 phase $Ge_{12}Li_x$ as a function of Li composition (x of tetragonal Ge_8Li_x and $2x/3$ of ST12 $Ge_{12}Li_x$). For pure Ge lattices, the diamond phase is more stable than the ST12 phase (Ge_{12}) by 1.12 eV (per Ge_8 stoichiometry). Remarkably, the ST12 $Ge_{12}Li_x$

becomes more stable than the same stoichiometric cubic phase as the Li composition increases ($x \geq 4$). Therefore, when a large number of Li atoms are involved in the discharge/charge cycles of LIB, the ST12 phase can serve as an active phase. The diamond structure is expected to eventually convert to a Li-intercalated ST12 structure because of its thermodynamic instability. The production of the ST12 Ge lattices contributes to enhanced LIB capacity due to the stronger binding interactions of Li atoms. Nevertheless, further investigation needs to explain why the production of ST12 phase is favored in the case of GeS NC.

At the low Li composition, the tetragonal phase is more stable than the ST12 phase since the E_{tot} value of Ge_8Li_2 is lower than the $2/3 \times E_{tot}$ value of $Ge_{12}Li_3$ by 0.17 eV. However, it should be noted that the total energy of the ST12 phase corresponds to the upper limit of the global energy minimum, whereas that of the tetragonal phase presumably corresponds to the global energy minimum. Therefore, the difference in the energy between the two phases can be <0.17 eV or even negative. In the same context, $Ge_{12}Li_{4.5}$ may be more stable than Ge_8Li_3 by an amount larger than the value that was calculated in this study. Evidently, the ST12 phase is more favorable than the tetragonal phase when the stoichiometry is higher than $Ge_{12}Li_3$ (or Ge_8Li_2). However, a clear conclusion cannot be drawn for the relative stability of tetragonal and ST12 structures at a lower Li composition.

CONCLUSIONS

The highly crystalline Ge, GeS, and GeO_2 NCs were synthesized conveniently using a gas phase laser photolysis reaction with TMG as the Ge precursor. The gas mixture with H_2S produced GeS NCs, and the oxidation of the Ge NCs produced GeO_2 NCs. The Ge, GeS, and GeO_2 NCs showed excellent cycling performances in LIB; the capacity was maintained at 1100, 1220, and 1100 mAh/g after 100 cycles, respectively. *Ex situ* XRD and TEM analyses revealed the production of metastable ST12 phase Ge upon the lithiation of Ge, GeS, and GeO_2 NCs, while no original phase remained. The crystalline features of ST12 Ge NCs persist even after 100 cycles. The more favorable production and persistence of the ST12 phase was observed for the GeS NCs (best candidate). First-principles calculations were performed for the stepwise Li insertion reaction of the ST12 (Ge_{12}) and diamond (Ge_8) phases. The ST12 $Ge_{12}Li_x$ structure at $x \geq 4$ is more stable than the same stoichiometric cubic phase (converted into the tetragonal phase). The $Ge_{12}Li_x$ lattices preserve the ST12 structure up to $x = 6$. In $Ge_{12}Li_3$, the Li atoms are preferentially placed on (100) planes, thus supporting the anisotropic lithiation behavior of the ST12 Ge NCs. The thermodynamic stability of the Li-intercalated ST12 Ge structures also explains why the delithiation does not lead to its conversion to the diamond phase. The stronger binding interactions of Li atoms within the ST12 Ge lattices contribute to enhanced cycling performance.

EXPERIMENTAL SECTION

Laser photolysis of tetramethyl germanium (TMG, Sigma-Aldrich) or a TMG/H_2S mixture was performed using a 1064 nm Nd:YAG pulsed laser (Coherent SL-10) operating with a repetition rate of 10 Hz and a pulse width of 10 ns. The precursors were degassed by several freeze (77 K)−pump−thaw cycles and then used without further purification. For the synthesis of Ge NCs, the vapors of TMG (20−50 Torr) were introduced into a 1 L pyrex glass reactor containing a gas valve connected to a standard vacuum line and a 2 in. diameter quartz optical window. The laser beam was focused into the closed reactor with a 10 cm focal length lens through the window. The experiment was carried out using a photon energy of 0.1−0.2 J/pulse. After 1 h of laser irradiation, the gas products were vented and the freestanding NC powders (mainly formed on the reactor wall) were collected by dispersing them in ethanol, followed by evaporation and vacuum drying at room temperature. A gas mixture of TMG (20 Torr) and H_2S (20 Torr) was typically used to synthesize the amorphous GeS NCs. For thermal annealing to produce the crystalline phase GeS, the amorphous NC powders were placed in a quartz tube at 450 °C under vacuum for 1 h. The GeO_2 NCs were synthesized by oxidation of Ge NCs at 600 °C for 1 h, under O_2 ambient.

The products were characterized by scanning electron microscopy (SEM, Hitachi S-4700), field-emission transmission electron microscopy (FE TEM, FEI TECNAI G2 200 kV and Jeol JEM 2100F), high-voltage transmission electron microscopy (HVEM, Jeol JEM ARM 1300S, 1.25 MV), and energy-dispersive X-ray fluorescence spectroscopy (EDX). Fast Fourier transform (FFT) images were generated by the inversion of the TEM images using Digital Micrograph GMS1.4 software (Gatan Inc.). High-resolution XRD patterns were obtained using the 9B and 3D beamlines of the Pohang Light Source (PLS) with monochromatic radiation. XRD measurement was also carried out in a Rigaku D/MAX-2500 V/PC using Cu Kα radiation ($\lambda = 1.54056$ Å).

For electrochemical tests, the electrodes of battery test cells were made of the active material (Ge, GeS, or GeO_2), Super P, and poly(acrylic acid) (PAA, 35 wt % dissolved in water; Aldrich) binder at a weight ratio of 6:2:2. The distilled water-mixed slurry was coated onto 20 μm thick Cu foil. The coated electrode was dried at 80 °C for 12 h and then roll-pressed. The coin-type half-cells (CR2032) prepared in a helium-filled glovebox contained an electrode, Li metal, microporous polyethylene separator, and electrolyte solution of 1 M $LiPF_6$ in 1:1:1 vol % of ethylene carbonate (EC)/ethyl methyl carbonate (EMC)/dimethyl carbonate (DMC). The performance of the cells was examined using a battery testing system (Maccor 4000) at a current density of 0.1 C between 0.01 and 1.5 V for 100 cycles. Cyclic voltammetry (CV) measurements were conducted (Biology SAS) using a voltage range of 0.01−2.5 V at a rate of 0.1 mV/s. For *ex situ* XRD measurements, the LIB half-cells charged or discharged to certain voltages were disassembled in a glovebox, and the electrodes were rinsed thoroughly with a DMC solution to remove the $LiPF_6$ salts.

For first-principles calculation of Li-intercalated Ge polymorphs, geometry optimizations were carried out using the Vienna *ab initio* simulation package (VASP).[43,44] Electron and ion interactions were described by the projector-augmented wave (PAW) method, which is essentially a frozen-core, all-electron calculation.[45] The Perdew−Burke−Ernzerhof (PBE) function was adopted for the exchange-correlation function.[46] For structure optimization, atoms were relaxed to the direction of the Hellmann−Feynman force using the conjugate gradient method until a stringent convergence criterion (0.03 eV/Å) was satisfied. The *k*-point sampling was done using a sufficient number of points. For example, 15 × 15 × 15 *k*-points were used for the cubic (diamond) structure, for which the optimized lattice constant was 5.78 Å. When Li atoms were intercalated, the diamond phase was found to change to a tetragonal phase. The binding energy (E_b) of Li atoms in a Ge crystal was calculated based on the chemical potential of a Li atom, which equated to its total energy in the body-centered cubic Li crystal with the optimized lattice constant. Therefore, the calculated E_b corresponds to the lower bound of the real binding energy, and the real binding energy will be larger than $|E_b|$ in magnitude.

Conflict of Interest: The authors declare no competing financial interest.

Acknowledgment. This study was supported by NRF (2011-001-5235; 2011-002-0090; 2011-001-3070; 2012-R1A1A-2039084) and WCU (R31-2012-000-10035-0). The HVEM (Daejeon) measurements were performed at the KBSI. The experiments at the PLS were partially supported by MOST and POSTECH. Computations were performed using a supercomputer at the Korea Institute of Science and Technology Information (KSC-2013-C2-014).

Supporting Information Available: XRD, EDX, and charge/discharge voltage profiles, and CV data. This material is available free of charge *via* the Internet at http://pubs.acs.org.

REFERENCES AND NOTES

1. St. John, M. R.; Furgala, A. J.; Sammells, A. F. Thermodynamic Studies of Li−Ge Alloys: Application to Negative Electrodes for Molten Salt Batteries. *J. Electrochem. Soc.* **1982**, *129*, 246–250.
2. Graetz, J.; Ahn, C. C.; Yazami, R.; Fultz, B. Nanocrystalline and Thin Film Germanium Electrodes with High Lithium Capacity and High Rate Capabilities. *J. Electrochem. Soc.* **2004**, *151*, A698–A702.
3. Chan, C. K.; Zhang, X. F.; Cui, Y. High Capacity Li Ion Battery Anodes Using Ge Nanowires. *Nano Lett.* **2008**, *8*, 307–309.
4. Park, M.-H.; Kim, K.; Kim, J.; Cho, J. Flexible Dimensional Control of High-Capacity Li-Ion-Battery Anodes: From 0D Hollow to 3D Porous Germanium Nanoparticle Assemblies. *Adv. Mater.* **2010**, *22*, 415–418.
5. Park, M.-H.; Cho, Y.; Kim, K.; Kim, J.; Liu, M.; Cho, J. Germanium Nanotubes Prepared by Using the Kirkendall Effect as Anodes for High-Rate Lithium Batteries. *Angew. Chem., Int. Ed.* **2011**, *50*, 9647–9650.
6. Wang, X.-L.; Han, W.-Q.; Chen, H.; Bai, J.; Tyson, T. A.; Yu, X.-Q.; Wang, X.-J.; Yang, X.-Q. Amorphous Hierarchical Porous GeO_x as High-Capacity Anodes for Li Ion Batteries with Very Long Cycling Life. *J. Am. Chem. Soc.* **2011**, *133*, 20692–20695.
7. Song, T.; Cheng, H.; Choi, H.; Lee, J.-H.; Han, H.; Lee, D. H.; Yoo, D. S.; Kwon, M.-S.; Choi, J.-M.; Doo, S. G.; *et al.* Si/Ge Double-Layered Nanotube Array as a Lithium Ion Battery Anode. *ACS Nano* **2012**, *6*, 303–309.
8. Tan, L. P.; Lu, Z.; Tan, H. T.; Zhu, J.; Rui, X.; Yan, Q.; Hng, H. H. Germanium Nanowires-Based Carbon Composite as Anodes for Lithium-Ion Batteries. *J. Power Sources* **2012**, *206*, 253–258.
9. Wang, J.; Du, N.; Zhang, H.; Yu, J.; Yang, D. Cu−Ge Core−Shell Nanowire Arrays as Three-Dimensional Electrodes for High-Rate Capability Lithium-Ion Batteries. *J. Mater. Chem.* **2012**, *22*, 1511–1515.
10. Xue, D.-J.; Xin, S.; Yan, Y.; Jiang, K.-C.; Yin, Y.-X.; Guo, Y.-G.; Wan, L.-J. Improving the Electrode Performance of Ge through Ge@C Core−Shell Nanoparticles and Graphene Networks. *J. Am. Chem. Soc.* **2012**, *134*, 2512–2515.
11. Jo, G.; Choi, I.; Ahn, H.; Park, M. J. Binder-Free Ge Nanoparticles−Carbon Hybrids for Anode Materials of Advanced Lithium Batteries with High Capacity and Rate Capability. *Chem. Commun.* **2012**, *48*, 3987–3989.
12. Gu, J.; Collins, S. M.; Carim, A. I.; Hao, X.; Bartlett, B. M.; Maldonado, S. Template-Free Preparation of Crystalline Ge Nanowire Film Electrodes *via* an Electrochemical Liquid−Liquid−Solid Process in Water at Ambient Pressure and Temperature for Energy Storage. *Nano Lett.* **2012**, *12*, 4617–4623.
13. Seng, K. H.; Park, M.-H.; Guo, Z. P.; Liu, H. K.; Cho, J. Self-Assembled Germanium/Carbon Nanostructures as High-Power Anode Material for the Lithium-Ion Battery. *Angew. Chem., Int. Ed.* **2012**, *51*, 5657–5661.
14. Xiao, Y.; Cao, M.; Ren, L.; Hu, C. Hierarchically Porous Germanium-Modified Carbon Materials with Enhanced Lithium Storage Performance. *Nanoscale* **2012**, *4*, 7469–7474.
15. Yuan, F.-W.; Yang, H.-J.; Tuan, H.-Y. Alkanethiol-Passivated Ge Nanowires as High-Performance Anode Materials for Lithium-Ion Batteries: The Role of Chemical Surface Functionalization. *ACS Nano* **2012**, *6*, 9932–9942.
16. Chockla, A. M.; Panthani, M. G.; Holmberg, V. C.; Hessel, C. M.; Reid, D. K.; Bogart, T. D.; Harris, J. T.; Mullins, C. B.; Korgel, B. A. Electrochemical Lithiation of Graphene-Supported Silicon and Germanium for Rechargeable Batteries. *J. Phys. Chem. C* **2012**, *116*, 11917–11923.
17. Rudawski, N. G.; Darby, B. L.; Yates, B. R.; Jones, K. S.; Elliman, R. G.; Volinsky, A. A. Nanostructured Ion Beam-Modified Ge Films for High Capacity Li Ion Battery Anodes. *Appl. Phys. Lett.* **2012**, *100*, 083111.
18. Kim, C. H.; Im, H. S.; Cho, Y. J.; Jung, C. S.; Jang, D. M.; Myung, Y.; Kim, H. S.; Back, S. H.; Lim, Y. R; Lee, C.-W.; *et al.* High-Yield Gas-Phase Laser Photolysis Synthesis of Germanium Nanocrystals for High-Performance Photodetectors and Lithium Ion Batteries. *J. Phys. Chem. C* **2012**, *116*, 26190–26196.
19. Yan, C.; Xi, W.; Si, W.; Deng, J.; Schmidt, O. G. Highly Conductive and Strain-Released Hybrid Multilayer Ge/Ti Nanomembranes with Enhanced Lithium-Ion-Storage Capability. *Adv. Mater.* **2013**, *25*, 539–544.
20. Seng, K. H.; Park, M.-H.; Guo, Z. P.; Liu, H. K.; Cho, J. Catalytic Role of Ge in Highly Reversible GeO_2/Ge/C Nanocomposite Anode Material for Lithium Batteries. *Nano Lett.* **2013**, *13*, 1230–1236.
21. Mullane, E.; Kennedy, T.; Geaney, H.; Dickinson, C.; Ryan, K. M. Synthesis of Tin Catalyzed Silicon and Germanium Nanowires in a Solvent-Vapor System and Optimization of the Seed/Nanowire Interface for Dual Lithium Cycling. *Chem. Mater.* **2013**, *25*, 1816–1822.
22. Kim, Y.; Hwang, H.; Lawler, K.; Martin, S. W.; Cho, J. Electrochemical Behavior of Ge and GeX_2 (X = O, S) Glasses: Improved Reversibility of the Reaction of Li with Ge in a Sulfide Medium. *Electrochim. Acta* **2008**, *53*, 5058–5064.
23. Cho, Y. J.; Im, H. S.; Myung, Y.; Kim, C. H.; Kim, H. S.; Back, S. H.; Lim, Y. L.; Jung, C. S.; Jang, D. M.; Park, J.; *et al.* Germanium Sulfide (II and IV) Nanoparticles for Enhanced Performance of Lithium Ion Batteries. *Chem. Commun.* **2013**, *49*, 4661–4663.
24. Bundy, F. P.; Kasper, J. S. A New Dense Form of Solid Germanium. *Science* **1963**, *139*, 340–341.
25. Joannopoulos, J. D.; Cohen, M. L. Electronic Properties of Complex Crystalline and Amorphous Phases of Ge and Si. I. Density of States and Band Structures. *Phys. Rev. B* **1973**, *7*, 2644–2657.
26. Liu, P.; Cao, Y. L.; Chen, X. Y.; Yang, G. W. Trapping High-Pressure Nanophase of Ge upon Laser Ablation in Liquid. *Cryst. Growth Des.* **2009**, *9*, 1390–1393.
27. Kim, S. J.; Quy, O. K.; Chang, L.-S.; Stach, E. A.; Handwerker, C. A.; Wei, A. Formation of the ST12 Phase in Nanocrystalline Ge at Ambient Pressure. *J. Mater. Chem.* **2010**, *20*, 331–337.
28. Yoon, S.; Park, C.-M.; Sohn, H.-J. Electrochemical Characterizations of Germanium and Carbon-Coated Germanium Composite Anode for Lithium-Ion Batteries. *Electrochem. Solid-State Lett.* **2008**, *11*, A42–A45.
29. Baggetto, L.; Notten, P. H. L. Lithium-Ion (De) Insertion Reaction of Germanium Thin-Film Electrodes: An Electrochemical and *In Situ* XRD Study. *J. Electrochem. Soc.* **2009**, *156*, A169–A175.

30. Li, J.; Dahn, J. R. An *In Situ* X-ray Diffraction Study of the Reaction of Li with Crystalline Si. *J. Electrochem. Soc.* **2007**, *154*, A156–A161.
31. Liu, X. H.; Huang, S.; Picraux, S. T.; Li, J.; Zhu, T.; Huang, J. Y. Reversible Nanopore Formation in Ge Nanowires during Lithiation−Delithiation Cycling: An *In Situ* Transmission Electron Microscopy Study. *Nano Lett.* **2011**, *11*, 3991–3997.
32. Liang, W.; Yang, H.; Fan, F.; Liu, Y.; Liu, X. H.; Huang, J. Y.; Zhu, T.; Zhang, S. Tough Germanium Nanoparticles under Electrochemical Cycling. *ACS Nano* **2013**, *7*, 3427–3433.
33. Liu, X. H.; Wang, J. W.; Huang, S.; Fan, F.; Huang, X.; Liu, Y.; Krylyuk, S.; Yoo, J.; Dayeh, S. A.; Davydov, A. V.; *et al. In Situ* Atomic-Scale Imaging of Electrochemical Lithiation in Silicon. *Nat. Nanotechnol.* **2012**, *7*, 749–756.
34. Liu, X. H.; Liu, Y.; Kushima, A.; Zhang, S.; Zhu, T.; Li, J.; Huang, J. Y. *In Situ* TEM Experiments of Electrochemical Lithiation and Delithiation of Individual Nanostructures. *Adv. Energy Mater.* **2012**, *2*, 722–741.
35. Lee, S. W.; McDowell, M. T.; Choi, J. W.; Cui, Y. Anomalous Shape Changes of Silicon Nanopillars by Electrochemical Lithiation. *Nano Lett.* **2011**, *11*, 3034–3039.
36. Zhang, Q.; Zhang, W.; Wan, W.; Cui, Y.; Wang, E. Lithium Insertion in Silicon Nanowires: An *Ab Initio* Study. *Nano Lett.* **2010**, *10*, 3243–3249.
37. Zhao, K.; Wang, W. L.; Gregoire, J.; Pharr, M.; Suo, Z.; Vlassak, J. J.; Kaxiras, E. Lithium-Assisted Plastic Deformation of Silicon Electrodes in Lithium-Ion Batteries: A First-Principles Theoretical Study. *Nano Lett.* **2011**, *11*, 2962–2967.
38. Yang, H.; Huang, S.; Huang, X.; Fan, F.; Liang, W.; Liu, X. H.; Chen, L.-Q.; Huang, J. Y.; Li, J.; Zhu, T.; *et al.* Orientation-Dependent Interfacial Mobility Governs the Anisotropic Swelling in Lithiated Silicon Nanowires. *Nano Lett.* **2012**, *12*, 1953–1958.
39. Cubuk, E. D.; Wang, W. L.; Zhao, K.; Vlassak, J. J.; Suo, Z.; Kaxiras, E. Morphological Evolution of Si Nanowires upon Lithiation: A First-Principles Multiscale Model. *Nano Lett.* **2013**, *13*, 2011–2015.
40. Nie, A.; Gan, L.-Y.; Cheng, Y.; Asayesh-Ardakani, H.; Li, Q.; Dong, C.; Tao, R.; Mashayek, F.; Wang, H.-T.; Schwingenschlögl, U.; *et al.* Atomic-Scale Observation of Lithiation Reaction Front in Nanoscale SnO_2 Materials. *ACS Nano* **2013**, *7*, 6203–6211.
41. Graetz, J.; Ahn, C. C.; Yazami, R.; Fultz, B. Electrochemical Characterizations of Germanium and Carbon-Coated Germanium Composite Anode for Lithium-Ion Batteries. *J. Electrochem. Soc.* **2004**, *151*, A698–A702.
42. Chockla, A. M.; Klavetter, K. C.; Mullins, C. B.; Korgel, B. A. Solution-Grown Germanium Nanowire Anodes for Lithium-Ion Batteries. *ACS Appl. Mater. Interfaces* **2012**, *4*, 4658–4664.
43. Kresse, G.; Hafner, J. *Ab Initio* Molecular Dynamics for Liquid Metals. *Phys. Rev. B* **1993**, *47*, 558–561.
44. Kresse, G.; Furthmuller, J. Efficient Iterative Schemes for *Ab Initio* Total-Energy Calculations Using a Plane-Wave Basis Set. *Phys. Rev. B* **1996**, *54*, 11169–11186.
45. Kresse, G.; Joubert, D. From Ultrasoft Pseudopotentials to the Projector Augmented-Wave Method. *Phys. Rev. B* **1999**, *59*, 1758–1775.
46. Perdew, J. P.; Burke, K.; Ernzerhof, M. Generalized Gradient Approximation Made Simple. *Phys. Rev. Lett.* **1996**, *77*, 3865–3868.